Acta Mater. 92, 2015, 163-177.
DOI:10.1016/j.actamat.2015.04.015
Preprint of paper as-accepted by journal.

Characterisation of radiation damage in W and W-based alloys from 2 MeV self-ion near-bulk implantations

Xiaoou Yi [a,b,*], Michael L Jenkins [c], Khalid Hattar [d], Philip D Edmondson [e] and Steve G Roberts [a,b]

[a] Department of Materials, University of Oxford, Parks Road, OX1 3PH, Oxford, U.K.
[b] CCFE, Culham Science Centre, Abingdon, OX14 3DB, Oxfordshire, U.K.
[c] Trinity College, University of Oxford, Broad Street, OX1 3BH, Oxford, U.K.
[d] Sandia National Laboratories, PO Box 5800 Albuquerque, NM 87185, U.S.A.
[e] Oak Ridge National Laboratory, 1 Bethel Valley Road, Oak Ridge, TN 37831, U.S.A.

* Corresponding author: xiaoou.yi@materials.ox.ac.uk

Abstract

The displacement damage induced in W and W-5 wt.% Re and W-5 wt.% Ta alloys by 2 MeV W^+ irradiation to doses 3.3×10^{17} - 2.5×10^{19} W^+/m^2 at temperatures ranging from 300 to 750°C has been characterized by transmission electron microscopy. An automated sizing and counting approach based on Image J (a Java-based image processing program developed at the National Institutes of Health) [1] has been performed for all near-bulk irradiation data. In all cases the damage comprised dislocation loops, mostly of interstitial type, with Burgers vectors **b** = ½<111> (> 60%) and **b** = <100>. The diameters of loops did not exceed 20 nm with most being ≤ 6 nm diameter. The loop number density varied between 10^{22} and 10^{23} loops/m^3. With increasing irradiation temperature, the loop size distributions shifted towards larger sizes, and there was a substantial decrease in loop number densities. The damage microstructure was less sensitive to dose than to temperature. Under the same irradiation conditions, loop number densities in the W-Re and W-Ta alloys were higher than in pure W but loops were smaller. In grains with normals close to **z** = <001>, loop strings developed in pure W at temperatures ≥ 500°C and doses ≥ 1.2 dpa, but such strings were not observed in the W-Re or W-Ta alloys. However, in other grain orientations complex structures appeared in all materials and dense dislocation networks formed at higher doses.

Keywords: W/W-alloys; Ion irradiation; Electron microscopy; Damage microstructure.

1. Introduction

The service environment of plasma-facing materials in future fusion reactors will be exceptionally severe. In particular, the divertor will operate at temperatures 1000-1300°C, at a thermal loading of ~10 MW/m^2 in ITER (former acronym of International Thermonuclear Experimental Reactor) and twice as much as this in commercial power reactors [2, 3]. W has been proposed as a primary candidate for this application, due to its high melting point, outstanding thermal conductivity and high threshold for sputtering [4]. However, the use of W will present great challenges: the divertor will experience high levels of displacement damage due to fast neutrons, typically measured in the number of displacements per atom (dpa) calculated from the NRT model [5] (100-150 dpa lifetime dose in a power station reactor); the production of helium by injection from the plasma and in (n, α) reactions; and the creation of transmutation products such as rhenium, osmium, and tantalum, which can form brittle precipitates in W [6-8]. All this will contribute to the hardening and embrittlement of W, which is already an intrinsically brittle material [9, 10].

Information on the radiation response of W is sparse. Researchers in Stuttgart including Häussermann, Wilkens, Rühle and Jäger performed thin-foil irradiations of pure W with 20-70 keV Au$^+$ ions at room temperature to doses below 10^{16} ions /m^2 [11-14]. The damage microstructure consisted predominantly of ½<111> loops of vacancy nature. Most loops were non-edge with habit planes close to {110}. A small number of faulted ½<110> loops and pure edge ½<111> loops were also present, but no <100> loops were found. The loops were produced at a dose where little or no cascade overlap occurs[1], suggesting that they result from the collapse of vacancy-rich cores within individual cascades. The loop geometries were consistent with nucleation by the Eyre-Bullough mechanism [15], which was originally postulated for the nucleation of interstitial loops in bcc metals. According to this mechanism, loops nucleate on the closest-packed {110} planes as faulted ½<110> loops. The stacking fault is then eliminated by a shear process through <100>, forming a perfect prismatic loop with **b** = ½<111>. The habit plane of the loop may subsequently rotate towards the pure edge orientation, i.e. from {110} to {111}, although loops may retain shear components. We found similar loop geometries in low-dose *in-situ* experiments on W, irradiated with 150 keV W$^+$ ions between room temperature and 800°C [16-18]. Loops were of vacancy type and most had **b** = ½<111> and many were non-edge. No faulted loops were found but we did find a small number of loops with **b** = <100>, which may have formed by the Eyre-Bullough mechanism. With increasing irradiation temperature, the fraction of pure edge ½<111> loops increased as sheared ½<111> loops and <100> loops became less common.

The results of these experiments are consistent with molecular dynamics simulations of collision cascades in W by Sand et al. [19], where both ½<111> and <100> loops were found in 150 keV W$^+$ cascades. No voids have yet been experimentally identified in low-dose heavy-ion irradiations of W [11, 12, 16, 18]. However, defect yields in W are small, so that most cascades do not collapse to loops [18]. It is possible that uncollapsed cascades contain small voids or vacancy complexes below the resolution limit of transmission electron microscopy. This possibility is suggested by recent calculations of the stability (relaxed formation energy) of various defect clusters in the nanometre range (i.e. < 10 nm) by Gilbert et al. [20]. The clusters considered included interstitial and vacancy loops with **b** = ½ <111>

[1] The threshold dose for cascade overlap can be either estimated from the quantity of defects with diameter, d, which a unit area could accommodate, or the critical dose beyond which the linear relationship between the defect number density and the dose is violated. The first approach is more commonly used, and the maximum observed defect size is often adopted as the diameter for threshold dose estimation [15].

as well as spherical voids. The most stable interstitial clusters were ½<111> loops, and the most stable vacancy clusters were spherical voids. A closed (fully collapsed) ½<111> vacancy loop may also exist, but is stable only above a critical diameter of ~3.4 nm [20]. In summary, the results above suggest that the formation of ½<111> and <100> vacancy loops seen in low-dose heavy-ion irradiation of W is an intrinsic cascade phenomenon, i.e. these loops are formed upon cascade nucleation, rather than by inter-/intra-cascade evolution.

Neutron-irradiation experiments carried out by Tanno et al. [21-24] and Hasegawa et al. [25, 26] have shed some light on the role of irradiation temperature, dose and presence of transmutation elements on the damage microstructural evolution as well as mechanical properties in W. These authors irradiated pure W and model W-(Re, Os) alloys in fission reactors (a sodium-cooled fast reactor JOYO; the Japan Material Testing Reactor - JMTR; the High Flux Isotope Reactor – HFIR, US) at temperatures between 400°C and 800°C to doses up to 1.54 dpa (1.2×10^{26} n/m^2, $E_n > 0.1$ MeV). The JOYO campaign focused on the impact of fast neutrons while the JMTR and HFIR campaigns were aimed at the consequences of high flux thermal neutrons (i.e. the transmutation of W of Re simultaneously with displacement damage). For pure W, the defect clusters in the JOYO batch consisted of a mixture of voids (>90%) and loops (< 10%). In addition, void lattices were observed at doses above 1 dpa for temperatures above 500°C. This is in good agreement with the earlier work of Sikka and Moteff, who also reported void lattices in W (550°C, 1.0×10^{26} n/m^2) [27]. Comparable conditions of irradiation temperature and dose did not replicate such phenomena in the HFIR batch. Instead, small quantities of voids and a dense population of needle-like precipitates (σ, ReW; χ, Re_3W) were observed. The presence of these brittle phases led to a remarkable hardening of W, i.e. by over a factor of 2 in Vickers hardness. For W-(3-26 wt.%)Re model alloys, the damage microstructure evolved differently in JOYO and HFIR, with regard to the effects of Re. In the JOYO batch, below 0.4 dpa, suppression of void production by Re was the dominant effect, and the radiation hardening was either comparable to or much less than in pure W. At higher doses, a steady increase of hardness with Re concentration was observed, associated with the nucleation of precipitates. In contrast, the nucleation of precipitates seemed continuous in the HFIR batch and the increase of hardening appeared almost proportional to the Re concentration. Similar damage features were also found in W-Os and W-Re-Os alloys [21-24].

The experiments described above have limitations in predicting the performance of W in a fusion reactor environment. Thin-film ion irradiation experiments allow cascade phenomena to be investigated, and beam lines incorporated with *in-situ* imaging facility may provide valuable insight into dynamic mechanisms such as loop interactions. However the presence of the foil surfaces (as found in thin-foil irradiation specimens or the back-thinned irradiated specimens) will have an effect on damage development [28], either pronounced or minor depending on the depth profile of the induced defects. The fission neutron experiments of Tanno et al. and Hasegawa et al. are better in this respect, although the relatively soft fission spectrum does not represent fully the effect of 14.1 MeV fusion neutrons. In addition these studies were limited in that they did not provide information on loop geometries, loop nature and relative loop populations. Furthermore, the matrix of irradiation conditions with respect to characterized material was incomplete, so that it was not possible to separate fully the influences of temperature and dose. A matrix of experimental parameters can be explored more easily by high-energy heavy-ion irradiations, which avoid the use of active specimens [29].

This paper describes the first systematic campaign to characterize the radiation damage in ~~bulk~~ W and W-Re and W-Ta alloys produced by high-energy (2 MeV) self-ion irradiations. Damage microstructures were analysed by diffraction contrast techniques in transmission electron microscopy. Defect configurations and geometries, and the sizes, number densities,

spatial distribution and nature of loops are catalogued with respect to irradiation temperature, dose, grain orientation and material composition. The role of each irradiation parameter on the damage microstructure in W is discussed explicitly.

2. Experiment

The materials investigated were pure W (typically 99.996 wt.%) and W-based alloys (5 wt.% Re, Ta) supplied by Plansee Gruppe, Austria. Prior to implantation, 3 mm TEM discs were spark-eroded from the as-received hot-worked materials. These were then thinned to 80-100 μm using diamond lapping films (with a final grit size of 1 μm), heat treated at 1400°C for 20 hours to remove dislocations, and electro-polished in baths of 0.5 wt.% NaOH aqueous solution for W and W-5Re (14 volts, 30-40 mA, close to 0°C) or 12.5 vol.% H_2SO_4 (98% grade), 1.5 vol.% HF in methanol for W-5Ta (8 volts, 30-40 mA, close to - 40°C) to achieve a mirror finish.

Self-ion implantations at $T \leq 500$°C were performed at the National Ion Beam Centre, University of Surrey (UK). Fig. 1 illustrates the geometry of implantations. A rastered beam of 2 MeV W^+ ions produced by a tandem Van de Graaff accelerator was directed in a vacuum chamber of ~ 10^{-6} Pa onto a heatable top-plate, on which was mounted the target holder (Fig. 1a). The irradiation temperature was controlled and calibrated by a thermocouple wire embedded in a rail (Fig. 1b). The range of uncertainty was estimated to be ± 25º. The dose and dose rates (≈ 3×10^{-4} dpa/s) were monitored and set by four Faraday cups located at each corner of the sample mask. A further irradiation at 750°C with 1.9 MeV W^+ ions was carried out at the Ion Beam Laboratory, Sandia National Laboratories (USA) using a broad continuous beam (Fig. 1d): these are treated as 2.0 MeV in this paper as the energy difference is not considered significant. A summary of irradiation conditions is shown in Table 1. The damage levels were assessed with SRIM 2013 for a pure W layer [30] following the suggestions made by Stoller et al. [31]. 5000 ions were run using the "Quick" Kinchin-Pease option, with the displacement threshold energy and the lattice binding energy set to 90 eV [32] and 0 [31] respectively. The number of displacements was then computed from the damage energy, using the NRT model [33]. The result of the simulations is shown in Fig. 1c for an ion dose of 10^{18} W^+/m^2. For other doses, the displacements per atom (dpa) simply scale up or down linearly. For all dpa values mentioned throughout the rest of the paper, we will be referring to the peak damage of the specimen. W-alloys were treated as pure W in the assessment of displacement damage, owing to the negligible change in density and the unavailability of displacement threshold energies as a function of Re/Ta concentration in W.

After ion irradiation, the implanted surface of each specimen was coated with a protective lacquer (Lacomit, Agar Scientific [34]) and it was back-thinned by jet electropolishing using the same recipes as described previously. On perforation the protective lacquer was removed with acetone. Flat regions of thickness ~ 100 nm were chosen for diffraction contrast microscopy. The standard methods used to determine loop Burgers vectors, habit planes and nature, and to count and size loops are described in [35], with further details of specific methods used in this work in Appendices 1-3. Measurements of the local foil thicknesses were performed by electron energy loss spectroscopy (EELS) [36], allowing defect volume number densities to be calculated. The effect of the foil surfaces was evaluated by Ferroni et al. [28], coupling treatments of glide and climb in dislocation dynamics modelling of radiation damage in thin foils of tungsten. The authors claimed that dislocation loops interact strongly with surfaces for depths < 3× the size of the loop. However, the range of the denuded zones near the surface in practice could be narrower due to the trapping of loops by small clusters and impurities. The larger the loop diameter, the stronger influence of trapping [37]. Here we provide a rough estimate of the total width of the denuded zones to be < 25 nm,

with regard to loops with diameter $d \leq 3$ nm. A quick check of this was performed near the foil edge or holes, where no defects were observed within the first extinction distance (200 kV, ξ_{110} = 24 nm [16]). According to the damage profile calculated by SRIM (Fig. 1c), in a typical specimen ~ 20% of the total displacement damage would be produced within these near-surface regions and the rest of the foil should be representative of the peak damage region. Hence, the overall microstructural trends reported in this paper can be considered as near-bulk material properties.

3. Results

3.1. General microstructures

Most grains in the annealed specimens had a normal close to **z** = <001> [17, 38, 39]. The general microstructural features are described first for such <001> grains and then for grains of other orientations.

Fig. 2 shows typical damage microstructures in <001> grains of pure W, W-5Re and W-5Ta at different irradiation temperatures and doses. All micrographs in this figure were recorded under two-beam kinematical bright-field conditions using a diffraction vector **g** = 200. In all cases the microstructure comprised small dislocation loops. In pure W, loops were on average larger and loop number densities lower with increasing in irradiation temperature. At a temperature of 500°C, considerably fewer loops are seen than at 300°C and the microstructure was more inhomogeneous, characterized by large rafts of loops with individual small loops embedded in the surrounding matrix. With increasing dose, loops appeared larger and loop number densities lower, but the effect is small, suggesting a saturation dose might apply. Similar but less pronounced trends with dose and temperature were identified in W-5Re and W-5Ta. However, the alloys contained randomly distributed loops, of higher number densities and smaller average size compared with equivalent irradiations of pure W.

The influence of grain orientation on damage microstructure is illustrated in Fig. 3, by comparing surface normal **z** = <001>, <011> and <111> grains of W-5Ta irradiated at 300°C. In non-<001> grains, strings of loops with **b** = ½<111> formed which evolved with increasing dose into complex networks. The mechanisms by which this occurs have been studied by *in-situ* observations and will be described in another paper [40], according to which the presence of a nearby free surface seems to favour the formation of loop strings in non-<001> grains by lowering the critical irradiation temperature and dose limit. From this perspective, the damage microstructural features in <001> grains are more likely to be representative of those formed by neutron irradiation with equivalent dose and temperature, where free surfaces would be far away. The quantitative analyses of damage microstructures in this paper will relate only to <001> grains.

3.2. Loop volume number densities

Loop volume number densities were deduced from measurements of foil thickness using EELS and areal number densities as found in weak-beam dark-field micrographs (taken using **g** = ± 200 and 020, 3-4**g**). The areas analysed were of relatively uniform thickness as indicated by thickness fringes. This allows the convenience of treating the foil volumes as 'cuboids'. The counting of loops was performed with the image analysis package Image J; details of the procedure are described in Appendix 1.

Fig. 4 presents the loop volume number densities in W and the alloys as a function of irradiation temperature and dose. For all materials:

1) With increasing irradiation temperature, the loop number density decreased. This trend was quite pronounced. In pure W, at a constant dose of 1.2 dpa, this trend appeared to be linear; the loop density decreased with increasing temperature at a rate of ~10^{20} loops/m^3/°C.
2) With increasing irradiation dose, the loop number density increased. This trend was weak. In particular at 300°C, an increase of dose by a factor of 75 just barely doubled the loop density. This is an indication that the damage in pure W may have saturated above 1.2 dpa at 300°C, and above 3.6 dpa at 500°C.

In W-5Re, higher densities of loops were observed than in pure W under the same irradiation condition. For example, at 300°C at a dose of 1.2 dpa, the increase loop density in W-Re was found to be ~1.7 times that in pure W. However, the effect of Re-alloying was much smaller at 500°C: the increase was barely noticeable at 0.4 dpa, and there was only a factor of ~1.4 increase at 1.2 dpa. The loop densities in W-Re saturated at around 1.2 dpa at 300°C and 3.6 dpa at 500°C. In W-5Ta, increases in loop density compared to pure W were larger than for W-5Re under all equivalent irradiation conditions. At 300°C at a dose of 1.2 dpa, the increase in loop density was by a factor of ~2.2. Even at 500°C the increase in loop density remained substantial, up to a factor of ~1.6. Due to the limited doses covered in these experiments, it has not yet been confirmed when damage saturates in W-5Ta.

3.3. Loop size analysis

Quantitative analysis of loop sizes in W and alloys were made using pairs of weak-beam dark-field (WBDF) images of the same areas of interest taken in **g** = ± 200 / 020, 3-4**g**. The method of sizing loops by treating them as particle-like objects can be found in Appendix 2, but the quality of the deconvolution of loop contrast intensities becomes problematic when dealing with doses > 1.2 dpa. Fig. 5 shows the loop size distributions for the various materials and irradiation conditions. Fig. 6 shows the fraction of loops larger than 4 nm in the different materials under different irradiation conditions. In pure W, loop sizes were more sensitive to irradiation temperature than to dose. At 300°C, the fraction of loops larger than 4 nm in pure W only changed from ~20 to ~25% when the dose was increased by a factor of 75. At 500°C, the trend is not as clear but again seems weak. However at a dose of 1.2 dpa, the fraction of loops larger than 4 nm at 750°C was double that at 300°C. In W-5Re the number of loops larger than 4 nm was generally smaller than in pure W under the same irradiation conditions, but showed similar trends with temperature and dose; the values for W-5Ta were indistinguishable from those for pure W under the same irradiation conditions for most cases.

3.4. Loop morphology

The procedure for determining loop geometries with good statistics in intermediate-dose irradiated materials is detailed in Appendix 3. The radiation damage microstructure of W and alloys featured a mixture of ½<111> and <100> loops. Fig. 7 demonstrates the co-existence of ½<111> loops (marked by circles) and <100> loops (marked by squares) in the case of pure W, irradiated at 750°C to a dose of 1.2 dpa.

Fig. 8 shows the fraction of ½<111> loops as a function of temperature and dose for the different materials. In pure W, the fraction of ½<111> loops appears to depend on irradiation temperature, increasing from ~ 79% to ~ 90% between 300°C and 750°C at a dose of 1.2 dpa. The fraction of ½<111> loops was however only weakly dependent on dose. In W-5Re the fractions of ½<111> loops were generally lower and depended less strongly on temperature than in pure W, and were largely independent of dose. In W-5Ta, the fraction of ½<111>

loops seemed to be independent of both irradiation dose and temperature and sat within a range of 80-85%.

3.5. Loop nature

The interstitial/vacancy nature of dislocation loops was determined manually from their inside-outside contrast behaviour [35], but this method is restricted to loops with diameters ≥ 4 nm. Smaller loops could not be analysed due to the difficulty in distinguishing inside contrast from outside contrast. The fraction of loops suitable for nature determination in different cases is therefore given by Fig. 6.

As shown in Fig. 8, damage microstructures in all materials contain at least 60% ½<111> loops, together with a minority of <100> loops. The analysis of the nature of the majority ½<111> loops is relatively straightforward in a **z** = [001] foil, since they all lie in so-called "safe" orientations, where loops with shear components show the same inside-outside behaviour as edge loops of the same Burgers vector [35]. Nature analyses of ½<111> loops were completed for all irradiated samples. However, the analysis of <100> loops is less straightforward. [100] and [010] loops with large edge components lie close to edge-on in the foil orientation [001]. In order to correctly deduce their nature, their sense of inclination under the imaging condition used for inside-outside analysis can only be found by the change in shape during high-angle tilting along a designated Kikuchi band. This was only possible for the largest <100> loops in pure W irradiated at 750°C to a dose of 1.2 dpa.

In order to demonstrate how the proportions of interstitial and vacancy loops vary in the different materials according to their size and the irradiation conditions, two types of plots were produced. Fig. 9 shows the fraction of interstitial loops among loops with **b** = ½<111>, as a function of irradiation temperature and dose. The error bars represent the number of loops in the analysed population which fell into the 4-5 nm size category. Fig. 10 and Fig. 11 show normalized size distributions, with the relative numbers of interstitial and vacancy loops in each size interval indicated.

The pure W data set is the most complete. The fraction of interstitial-type loops among ½<111> loops was found to be over 50% under all irradiation conditions. The fraction of interstitial loops increased (up to ~ 95%) with both irradiation temperature and dose between 300°C and 500°C but no further increase was found in the specimen irradiated at 750°C to 1.2 dpa. At 300°C, a dose increase by a factor of 3 had little effect on loop sizes (see also Fig. 5), but the fraction of interstitial-type loops increased significantly. At 500°C, the loop size distributions began to flatten out and the peak size category shifted towards larger sizes. As the dose increased at 500°C, vacancy-type loops disappeared from the loop populations. If present at all, vacancy loops did not exceed 9 nm in size, whilst interstitial loops in the > 10 nm size category were present in considerable numbers. At 750°C, the size distribution of analysed ½<111> loops flattened out further compared with irradiations at 500°C. The number of loops of size > 9 nm nearly doubled and vacancy-type loops were found in the > 10 nm size category. The statistics for <100> loops are poor since only ten were analysed in total, but of these nine were found to be of interstitial type.

The nature analyses of ½<111> loops in W-5Re and W-5Ta (Fig. 11) revealed two common features: (1) at constant irradiation temperature, an increase in dose had little effect on the fraction of interstitial loops; (2) at 300°C, the fractions of interstitial loops in the alloys was higher than in pure W, while at 500°C the opposite was the case. In W-5Re, the fraction of interstitial loops decreased from ~80% to ~70% between 300°C and 500°C. In W-5Ta, the fraction of interstitial loops was ~75%, independent of temperature. The loop size - nature plots show that the fraction of loops in the 5-6 nm size category increased gradually with temperature and dose in both W-5Re and W-5Ta. This increase is largely due to an increase

in the number of vacancy-type loops in this size category, as opposed to the trend for elimination of vacancy loops in pure W.

4. Discussion

4.1. The role of irradiation temperature

The irradiation temperature has a substantial influence on the evolution of radiation damage microstructure in W, even at temperatures less than 30% of the melting temperature of W (3422°C). We will discuss its impact on the geometry of loops, the number density and size of loops, and finally the nature of loops.

Two types of dislocation loops have been observed in self-ion damaged W, with Burgers vectors **b** = ½<111> and **b** = <100>. The predominance of loops with **b** = ½<111> is consistent with the results of others [12, 16]. DFT calculations of loop formation energy show that at 0 K, interstitial loops with **b** = ½<111> are of lower energy than loops with **b** = <100> for cluster sizes up to 276 SIAs, corresponding to loop diameters of approximately 4.5 nm for ½<111> loops and 4.2 nm for <100> loops. The free-energy of loops increases with temperature, and at a more rapid rate for <100> loops than ½ <111> loops. At temperatures above 450 K, which applies to all irradiations in this paper, loops with **b** = ½<111> were predicted to be energetically more favourable than loops with **b** = <100> throughout the entire size range [41]. A similar trend was found for vacancy loops. The origin of metastable <100> geometries still remains controversial. Some have considered that <100> loops are the collision product of two ½<111> loops [42, 43] and some have claimed they could be formed directly during the non-equilibrium cascade process [19].

The role of irradiation temperature on the loop number densities, sizes and nature in W is associated with the mobility and interaction of point defects and clusters. The range of temperature investigated in this paper corresponds to three annealing stages as defined by the recovery of fast neutron damage in W, i.e. stage II (-170°C ~ 350°C), stage III (350°C ~ 640°C) and stage IV (640°C ~ 970°C) [44]. Recent in-situ annealing work confirmed this for self-ion damage in W [45]. The escape of SIAs from traps such as impurities and dislocations is considered responsible for stage II recovery. Vacancies become significantly mobile between 350°C ~ 640°C and this accounts for stage III recovery [46]. The mechanism for stage IV remains controversial. Some attribute this stage to the migration of vacancy clusters and vacancy-impurity complexes [47].

Damage evolution in stage II irradiations largely involves the growth of interstitial clusters towards visible loops and the disappearance of smaller clusters in favour of larger ones; clusters of interstitials, including small loops, may be produced directly within cascades [19]. DFT calculations suggest that the binding energies of small SIA clusters are high, e.g. the binding energy for a 7-SIA cluster is around 6.16 eV [48]. Small interstitial clusters and loops are also highly mobile [49]. The growth of such stable clusters is likely to be governed by mutual elastic interactions leading to coalescence, rather than by Ostwald ripening [48, 50, 51]. Indeed, coalescence of small mobile interstitial loops has been seen directly in our *in-situ* experiments [17]. Vacancy loops have also been identified at this stage. Since monovacancies are not significantly mobile at these temperatures, these loops must originate from cascade processes. Evidence for cascade collapse to vacancy loops has been found in both *in-situ* W^+ ion irradiations [16] and molecular dynamic simulations of high energy collision cascades in W [19], although the probability of cascade collapse is small. At 300°C, the diffusivity of a vacancy loop (**b** = ½<111>, 3.7 nm in diameter) in W is about an order of magnitude less than that of an interstitial counterpart [49]. However this might still allow some growth of vacancy clusters by the same mechanism as interstitial clusters, i.e. loop coalescence through elastic interactions [18]. Overall, visible vacancy loops might be

expected to be present in smaller numbers and sizes than the dominant population of visible interstitial loops, consistent with our observations.

In stage III, monovacancies become mobile. This favours the recombination of SIAs and vacancies, as well the absorption of migrating vacancies by large clusters which leads to growth of vacancy clusters or shrinkage of interstitial clusters. In addition, glide of both interstitial and vacancy loops occurs more easily [50]. Thus, mobile point defects and defect clusters would be able to interact strongly through their elastic strain fields, coalesce, and give rise to the accelerated increase in loop size and the decrease in loop number density (Fig. 4 and Fig. 10). The impact of the widened gap in diffusivity between interstitial and vacancy loops during this stage [49] is reflected in the increased fraction of large interstitial loops from 300°C (stage II) to 500°C (stage III), as seen in Fig. 9 and Fig. 11.

At still higher temperatures, corresponding to the irradiation at the upper regime of stage IV, microstructural development appears to be dominated by interactions between increasingly mobile loops and clusters. At this stage, spatial ordering of loops into strings and rafts occurs in pure W ($\mathbf{z}$ = <001>), due to elastic interaction of interstitial loops with the same Burgers vector variant [53] This process has been seen directly in *in-situ* irradiations [17]. The increased mobility of vacancy clusters and vacancy-impurity complexes at these temperatures is probably responsible for the presence of a small number of large vacancy loops by the coalescence of smaller loops [49] (also refer to section 4.5.).

4.2. The role of irradiation dose

In the low dose range (0.4 - 1.2 dpa), loop number densities seemed to increase with dose. However, saturation of damage occurred above a critical dose level, the value of which decreased with temperature. This may be explained as follows. SIA and vacancy clusters are produced continuously in displacement cascades. These may nucleate new loops or be lost at existing loops by absorption or coalescence. Initially the nucleation rate of clusters exceeds the annihilation rate. At the critical dose level, the two competing processes approach a state of balance.

An increase in dose (up to a factor of 9 in this work) also led to an increase in the size of interstitial ½<111> loops, along with the shrinkage and loss of vacancy loops. Qualitatively an increase of loop sizes with dose may be understood as a consequence of the reduction in the average distance between clusters. Existing defect clusters may gain in size by attraction and absorption of newly-introduced clusters of the same nature or shrink by absorbing clusters of the opposite nature. The range of motion of mobile loops of either nature may be restricted by the nucleation of new obstacles on their glide paths. Overall the damage evolution is likely to be controlled by the more mobile interstitial loops, leading to interstitial loop growth and vacancy loop shrinkage. Current interstitial loop growth models seem limited in describing this scenario quantitatively. The model of Kiritani et al. [52] for interstitial loop growth under electron irradiation is essentially a 3D diffusion model [53], based on the assumption that point defects are the main mobile defects, which is reasonable for electron irradiation where defects are introduced as Frenkel-pairs, but may not be the case for cascade-producing irradiation. The work of Woo and Semenov [54] considered loop growth under cascade damage conditions and introduced a production bias of intra-cascade interstitial and vacancy clusters. However, their model did not account for the presence of vacancy loops, and vacancies were assumed to accumulate at voids. Interstitial loops always grow in the presence of voids, in order to counter-balance the increased volumetric strain [55].

4.3. The role of grain orientation

Damage microstructures in three grain normal orientations have been compared in this paper, namely **z** = <001>, <011> and <111>. In <001> grains, strings and rafts of loops developed in pure W only at temperatures above 500°C or doses above 1.2 dpa. In the other grain orientations, loop strings formed at 300°C in both pure W and the alloys. An increase in dose then facilitated the evolution of loop strings to more complex networks. Such types of "self-ordered defect structures" have been reported previously in W (4 keV Ar^+, **z** = <001> grain, $\Phi \geq 2.0 \times 10^{19}$ Ar^+/m^2) [56] as well as other cubic metals/alloys, both in thin-foil and bulk specimens [57, 58]. Strong elastic interactions and the trend to minimize stress caused by a high density of defects have been argued to be the driving force for such phenomena [59]. With regard to the role of grain orientations found in this work, one likely explanation is the effect of surface traction [60]. In a [001] grain, the probability of loop loss through glide is equal for all variants of ½<111> loops, whereas in [011] grains, say, loops with **b** = $\pm\frac{1}{2}[11\bar{1}]$ and $\pm\frac{1}{2}[\bar{1}1\bar{1}]$ have no component of **b** towards the surface and so would be retained in the foil. In a [111] grain, loops with **b** = ½[111] would be lost preferentially. The more limited variety of loop geometries in these cases may favour the formation of strings and rafts of loops with the same Burgers vector.

4.4. The role of alloying elements

Direct observations of loop motion during *in-situ* irradiations of W and W-5Re suggest that Re atoms hinder the migration of loops, especially interstitial loops which are very mobile in pure W [16]. Further evidence that alloying elements restrict the mobility of loops is found in the size-nature plots of Fig. 10 and Fig. 11, in which large interstitial loops occur less frequently in W-5Re and W-5Ta than in pure W, suggesting that loop coalescence is less likely in the alloys. This conclusion is consistent with DFT calculations [61] which show that the binding energy between Re atoms and <111> crowdions in W is positive and quite large (max. 0.9 eV), implying that Re atoms may effectively trap SIA defects. Similar calculations show that Ta atoms repel SIA defects with slightly weaker strength (max. 0.6 eV) [61], and so will also retard SIA mobility. Lower loop mobilities can explain the effect of alloying on loop number densities and sizes, and the suppression of string and raft formation. The higher loop number densities found in W-5Ta compared to W-5Re is in agreement with the enhanced radiation hardening effect found in nanoindentation tests on W-5Ta compared to W-5Re (using the same materials and irradiations as for the materials studied here) [38, 39]. However, results of the binding energy calculations suggest a larger extent of hardening in W-5Re than in W-5Ta where loop trapping would be more effective [61]. The origin of this apparent inconsistency might be that the pinning objects are not individual Re or Ta atoms, but small clusters of these atoms. 3D atom-probe tomography on the 2 MeV W^+ ion irradiated W-5Re samples has found increased clustering of Re at loop perimeters with increasing dose [38].

4.5. On the formation of large vacancy loops

From a theoretical standpoint, an explanation for the formation of large vacancy loops (diameter ≥ 6 nm) encounters the following two challenges. First, the mobility of monovacancies is restricted. It is well established that the vacancy migration energy in W is large (1.78 eV) [55]. Even in the temperature range between 500°C and 750°C when vacancies gain increased mobility, the amount of vacancy loop growth found experimentally is considerably higher than the theoretical prediction, as reported by Mason et al. [18]. Second, at all temperatures vacancy loops have a bias for absorption of interstitials [62], and so would be expected to shrink by absorbing excess interstitials.

Hence, an alternative growth mechanism must be responsible for the formation of large vacancy loops. Electron irradiations of zirconium suggest that stress relief may be a cause. Griffiths et al. reported that where there was an energy gain to the system, vacancy loops nucleate and grow to relieve an appropriate stress [63, 64]. Similar observations were also found in neutron irradiated molybdenum and its alloy TZM (Mo, 0.5 wt.% Ti, 0.1 wt.% Zr). Vacancy loops nucleated and grew at the sites of voids, which shrank. These loops act as biased sinks which attract SIAs (which are associated with large strain fields) [65]. A further possible explanation for vacancy loop growth was suggested by a modelling study by Mason et al. [18], where loop-loop and loop-void long-range elastic interactions on top of monovacancies migration were responsible for vacancy loop growth.

Finally, the fate of large vacancy loops seems to be dependent on the irradiation condition and material composition. Increasing irradiation temperature stabilizes large vacancy loops by facilitating their coalescence with small vacancy clusters. Alloying with Re and Ta also stabilizes large vacancy loops, possibly through segregation as suggested by electron irradiations on zirconium [63, 64]. However, an increase in dose results in the shrinkage and eventual elimination of large vacancy loops.

5. Summary and conclusions

W and W alloys (5 wt.% Re, Ta) were implanted with 2 MeV W^+ ions over a dose range of 3.3×10^{17} - 2.5×10^{19} W^+/m^2 (0.4 -30 dpa) at temperatures between 300°C and 750°C. Electron microscopy studies of the damage microstructure show:

1. Dislocation loops with **b** = ½<111> (> 60%) and **b** = <100> coexisted in all materials and for all irradiation conditions studied, the majority being of interstitial type. The diameter of loops did not exceed 20 nm, with the most frequent size being ≤ 6 nm. The loop number density varied between 10^{22} and 10^{23} per m^3.
2. In surface normal **z** = <001> grains of pure W, increases in both temperature and dose facilitated loop growth. Loop number density dropped with increasing temperature (up to ~ 70%), the range of which corresponded to three annealing stages of W. Within each annealing stage, there was an indication that loop number densities followed the increase of dose, however the saturation of loop population was observed above temperature-dependent critical doses. Higher irradiation temperatures also favoured a change in damage microstructure from a randomly distributed body of loops to a mixture of large rafts of loops and isolated small loops. The onset temperature for this was around 500°C.
3. In **z** = <001> grains of W-5Re and W-5Ta, the spatial distributions of loops were random. Loop number densities in both alloys were higher than in pure W, and higher in W-5Ta than in W-5Re. Re and Ta additions both suppressed the growth of loops by restricting their mobility. Alloy atoms may also segregate at the dislocation loops, stabilizing the vacancy loops in particular. The overall loop Burgers vector distribution and fraction of interstitial loops appeared independent of irradiation conditions.
4. The spatial distribution of loops in **z** = <001> grains was found to be different from those in <011> and <111> grains. In the <001> case, strings or rafts of loops were found only in pure W above 500°C or 1.2 dpa. In grains of the other orientations, complex damage structures formed not only in all materials, but also at lower temperatures. The effect of the preferential loss of loop variants to the surface in different grain orientations may be responsible for the phenomenon.

Acknowledgements

The irradiations were carried out at the Surrey Ion Beam Centre (Surrey-IBC, UK), and the Ion Beam Laboratory, Sandia National Laboratories (USA). We thank Dr. Nianhua Peng (Surrey-IBC) for assistance with the 2 MeV W^+ ion irradiations, and Prof. C. A. English (National Nuclear Laboratory, UK),Prof. S. L. Dudarev, Dr. D. Nguyen-Manh, Dr. D. R. Mason and Dr. M. R. Gilbert (Culham Centre for Fusion Energy, UK) for inspiring discussions. We acknowledge the Division of Materials Science and Engineering, Office of Basic Energy Sciences, U.S. Department of Energy for the 1.9 MeV W^+ ion irradiation. Sandia National Laboratories is a multi-program laboratory managed and operated by Sandia Corporation, a wholly owned subsidiary of Lockheed Martin Corporation, for the U.S. Department of Energy's National Nuclear Security Administration under contract DE-AC04-94AL85000. XY acknowledges funding support the Culham Centre for Fusion Energy via a Research Fellowship at St. Edmund Hall, University of Oxford and the EPSRC, via the programme grant 'Materials for Fusion and Fission Power', EP/H018921/1.

Appendix: Notes on data processing with Image J

1. The counting of loops

The counting of loops assumes that each local intensity maximum on the micrograph represents a loop. The software finds the local maxima by acquiring a noise tolerance parameter, measured in grey scale. Maxima are therefore ignored if they do not stand out from the surroundings by more than this parameter. In practice, the value is chosen arbitrarily, winded down gradually from 255 (the maximum intensity in grey scale). During each step, a judgment is made by eye whether all loops have been picked up. The process is iterated until all loops are counted. An uncertainty in counts arises when dealing with loops with intensities comparable to that of the background noise. The range of uncertainty is estimated from the fluctuation of the background intensity. Fig. 12 a) and b) illustrates the estimation. A loop-free area (as judged by eye) is selected and a line is drawn (Fig. 12 a). Then, an intensity profile along this line is generated as shown in Fig. 12 b). The magnitude of the grey scale fluctuation is around 10. Hence, the noise tolerance parameter is also assigned with a ±10 variation. If one defines the grey scale intensity of a loop comparable to that of the background as I, then loop counts corresponding to noise tolerance parameters I-10 and I+10 are made. The difference between the counts represents the range of uncertainty. The same noise tolerance parameter value has been assigned for all counting of loops in this paper, since all micrographs adopted for loop number density analysis were recorded under weak-beam dark-field conditions (**g** = ± 200/020, 3-4**g**) with 5s exposure on a Philips CM 20 microscope on negatives. This weak condition was chosen so that defects could be easily seen and recorded [66]. It is also very convenient to set-up and switch from the corresponding kinematical bright-field condition. Weaker conditions require longer exposure time and would pose quite a challenge for the stage stability. At least 4 images were considered for each data point on the loop density plot (Fig. 4), each cropped to ~ 500 nm by 500 nm from the original micrographs to avoid complex backgrounds like thickness contours.

2. Loop size distributions

The image sizes of loops may vary with the diffraction conditions. Quantitative analyses of loop size distributions in this paper were averaged among data obtained from 2 to 4 pairs of weak-beam dark-field micrographs of the same areas of interest taken in **g** = ± 200/020, 3-

4**g**. Processed in pairs, e.g. **g** = ± 200 for region ***n***, the micrographs were first converted from grey scale to a binary format. Each visible loop was assumed to be a particle-like feature possessing a circularity value between 0 (infinitely elongated polygon) and 1 (perfect circle) [1]. The range of loop dimensions was binned at a step size of 1 nm for loops between 1 and 10 nm, and all loops larger than 10 nm were grouped as one category. As a consequence of the difficulty of distinguishing loop boundaries from the background noise (or resolution limit of diffraction contrast), loops that were smaller than 1 nm were not taken into account in the overall size distribution analyses. Loop sizes (***d***) were then converted from the range of areas (***A***) equivalent in (pixel)^2 for all particle-like objects picked up by the software, following $d = \sqrt{4A/\pi}$. Depending on the circularity of each particle-like object, ***d*** represents either the true diameter or the equivalent diameter. For each pair of micrographs of the same region, loop population would be identical, but the size distribution would be affected by the inside-outside contrast, i.e. the image size would be either smaller or larger than the true size. Loop counts within each binned category were therefore averaged with this respect and normalized against the total loop population in the region. We repeated the procedure for other ± **g** pairs and regions. Finally, the averaged (normalized) frequency of occurrence for each bin was calculated with regard to all ± **g** pairs considered and plotted in Fig. 5. The error bars show the standard deviation of the frequency in each bin.

Despite the convenience in loop sizing following this automated procedure, a few cautionary points must be born in mind in the interpretation of the acquired loop size measurements. First, in the conversion of raw grey scale data to binary format (foreground 255, background 0), any intensity less than an automated threshold[2] (computed based on the isodata algorithm developed by Ridler and Calvard [67]) is taken as 0 after the conversion. Fig. 13 demonstrates the conversion of image formats with two examples, i.e. a large/bright loop (~ 6 nm) and a small/faint loop (~ 2 nm) seen in irradiated pure W. The original grey scale image and respective 3D surface profiles of selected loops in grey scale and binary format are shown from a) to e). The boundaries of loop are defined as points where the grey scale intensity shows a sharp change in gradient. In the case of a large/bright loop, the systematic error in loop sizing due to image conversion is ~10%. However, when the same intensity threshold is used for small/faint loops, the systematic underestimation of loop size is larger at ~ 35%. Generally, size measurements following this method can be regarded as accurate reproductions of the true image size for loops larger than 4 nm.

The second point to bear in mind is the challenge of sizing individual loops at high doses. The separation distance among loops may be so small that they are mistaken for one single large loop. This may be the major cause for the large standard deviations found in overall loop size distributions presented in this paper. Finally, one needs to note that only one diffraction condition was adopted for sizing analysis and the size distributions shown do not distinguish between loops of type ½<111> or <100>. All variants of ½<111> loops would have been visible in either **g** = ±200 or **g** = ±020 while loops of <100> would have been present in only one of the **g** pairs. Image size changes due to inside-outside contrast would have been averaged out for both loop populations.

[2] The isodata algorithm of automatic thresholding
The grey scale histogram is initially segmented into a foreground part (also known as object) and a background part using a starting threshold value, e.g. half the maximum dynamic range. Then, the averages of the pixels at or below the threshold and pixels above are computed. The averages of those two values are then calculated. The threshold is then incremented and the process repeats until the following relation is satisfied:
threshold > ½ (average foreground + average background).

3. Loop Burgers vectors analysis

The Burgers vectors of dislocation loops are best determined by one-to-one correlation of individual loop images under several diffraction conditions, and looking invisible or weak in contrast. Owing to the high loop number densities, which made one-on-one correlation impractical, this method was not viable in this paper. Instead the numbers of loops with ½<111> and <100> Burgers vectors were extracted by analysing the numbers of loops seen in micrographs taken with **g** = ± 200 / 020 and **g** = $\pm 110/\ 1\bar{1}0$, and assuming that all variants of ½<111> and <100> loops occur equally. It is further assumed that loops will not be seen in a given micrograph if the invisibility criterion **g.b** = 0 holds [68]. If the number of loops of any ½<111> variant present in the area of interest is assigned x, and that of any <100> variant y, then we would expect to see a total of (4x+y) loops in micrographs obtained in **g** = ± 200 / 020 and (2x+2y) loops in micrographs obtained in **g** = $\pm 110/\ 1\bar{1}0$ respectively. By counting the total number of loops visible in each micrograph x and y can be found. Typically a total of eight micrographs were recorded for each **g** and its equivalents to improve the statistics. The fraction of ½<111> loops in the total population is then 4x/(4x+3y), which has been plotted against irradiation temperature and dose in Fig. 6. This non-standard approach of extracting Burgers vectors among a dense population of loops was originally found in works on neutron irradiated Fe-Mn alloys [69]. A recent publication on ion irradiated Fe and Fe-Cr alloys elaborated the method further, where the loss of different variants of ½<111> loops to the foil surface were assigned with a weighted probability [70]. This is particularly important when the grain orientation is not **z** = <001>, unlike the common case in this paper.

References

[1] Image Processing and Analysis in Java, National Institute of Health: http://imagej.nih.gov/ij/index.html.
[2] G. McCracken, P. Scott, Fusion: The Energy of the Universe, Second ed., Academic Press, Elsevier, Waltham & Oxford, 2013.
[3] V. Barabash, G. Federici, J. Linke, C.H. Wu, Material/plasma surface interaction issues following neutron damage, J. Nucl. Mater. 313-316 (2003) 42-51.
[4] M. Rieth, J.L. Boutard, S.L. Dudarev, T. Ahlgren, S. Antusch et al, Review on the EFDA programme on tungsten materials technology and science, J. Nucl. Mater. 417 (2011) 463-467.
[5] M.J. Norgett, M.T. Robinson, I.M. Torrens, A proposed method of calculating displacement dose rates, Nuclear Engineering and Design 33 (1975) 50-54.
[6] M.R. Gilbert, S.L. Dudarev, S. Zheng, L.W. Packer, J.-C. Sublet, An integrated model for materials in a fusion power plant: transmutation, gas production, and helium embrittlement under neutron irradiation, Nucl. Fusion 52 (2012) 083019.
[7] G.A. Cottrell, R. Pampin, N.P. Taylor, Transmutation and phase stability of tungsten armor in fusion power plants, Fusion Sci. Technol. 50 (2006) 89-98.
[8] M.R. Gilbert, J.-C. Sublet, Neutron-induced transmutation effects in W and W-alloys in a fusion environment, Nucl. Fusion 51 (2011) 043005.
[9] A. Giannattasio, S.G. Roberts, Strain-rate dependence of the brittle-to-ductile transition temperature in tungsten, Philos. Mag. 87 (2007) 2589-2598.
[10] D.E.J. Armstrong, P.D. Edmondson, S.G. Roberts, Effects of sequential tungsten and helium ion implantation on nano-indentation hardness of tungsten, Appl. Phys. Lett. 102 (2013) 251901.

[11] F. Häussermann, A study of the radiation damage produced by energetic gold ions in molybdenum and tungsten, Philos. Mag. 25 (1972) 583-598.
[12] F. Häussermann, Analysis of dislocation loops in tungsten produced by 60keV ion irradiation, Philos. Mag. 25 (1972) 561-581.
[13] F. Häussermann, M. Rühle, M. Wilkens, Black-white contrast figures from small dislocation loops II. Application of the first order solution to small loops in ion-irradiated tungsten foils, Phys. Stat. Sol. (b) 50 (1972) 445-457.
[14] W. Jäger, M. Wilkens, Formation of vacancy-type dislocation loops in tungsten bombarded by 60 keV Au ions, Phys. Stat. Sol. (a) 32 (1975) 89-100.
[15] B.L. Eyre, R. Bullough, On the formation of interstitial loops in b.c.c. metals, Philos. Mag. 12 (1965) 31-39.
[16] X. Yi, M.L. Jenkins, M. Briceno, S.G. Roberts, Z. Zhou, M.A. Kirk, In situ study of self-ion irradiation damage in W and W-5Re at 500 °C, Philos. Mag. 93 (2012) 1715-1738.
[17] X. Yi. Electron Microscopy Study of Radiation Damage in Tungsten and Alloys. Materials, Doctor of Philosophy: University of Oxford, 2013.
[18] D.R. Mason, X. Yi, M.A. Kirk, S.L. Dudarev, Elastic trapping of dislocation loops in cascades in ion-irradiated tungsten foils, J. Phys: Condens. Matter 26 (2014) 375701.
[19] A.E. Sand, S.L. Dudarev, K. Nordlund, High-energy collision cascades in tungsten: Dislocation loops structure and clustering scaling laws, EPL 103 (2013) 46003.
[20] M.R. Gilbert, S.L. Dudarev, P.M. Derlet, D.G. Pettifor, Structure and metastability of mesoscopic vacancy and interstitial loop defects in iron and tungsten, J. Phys: Condens. Matter 20 (2008) 345214.
[21] T. Tanno, A. Hasegawa, J.-C. He, M. Fujiwara, S. Nogami, Effects of transmutation elements on neutron irradiation hardening of tungsten, Mater. Trans. 48 (2007) 2399-2402.
[22] T. Tanno, A. Hasegawa, J.C. He, M. Fujiwara, M. Satou, S. Nogami, K. Abe, T. Shishido, Effects of transmutation elements on the microstructural evolution and electrical resistivity of neutron-irradiated tungsten, J. Nucl. Mater. 386-388 (2009) 218-221.
[23] T. Tanno, M. Fukuda, S. Nogami, A. Hasegawa, Microstructure development in neutron irradiated tungsten alloys, Mater. Trans. 52 (2011) 1447-1451.
[24] T. Tanno, A. Hasegawa, M. Fujiwara, J.-C. He, S. Nogami, M. Satou, T. Shishido, K. Abe, Precipitation of Solid Transmutation Elements in Irradiated Tungsten Alloys, Mater. Trans. 49 (2008) 2259-2264.
[25] A. Hasegawa, M. Fukuda, S. Nogami, K. Yabuuchi, Neutron irradiation effects on tungsten materials, Fus. Eng. Des. 89 (2014) 1568-1572.
[26] A. Hasegawa, T. Tanno, S. Nogami, M. Satou, Property change mechanism in tungsten under neutron irradiation in various reactors, J. Nucl. Mater. 417 (2011) 491-494.
[27] V.K. Sikka, J. Moteff, Superlattice of voids in neutron‐irradiated tungsten, J. Appl. Phys. 43 (1972) 4942-4944.
[28] F. Francesco, T. Edmund, F. Steven, Dislocation dynamics modelling of radiation damage in thin films, Modelling Simul. Mater. Sci. Eng. 22 (2014) 045009.
[29] G.S. Was, Fundamentals of Radiation Materials Science: Metals and Alloys, First ed., Springer-Verlag, Berlin & Heidelberg, 2007.
[30] R.S. Averback, Ion-irradiation studies of cascade damage in metals, J. Nucl. Mater. 108 & 109 (1982) 33-45.
[31] R.E. Stoller, M.B. Toloczko, G.S. Was, A.G. Certain, S. Dwaraknath, F.A. Garner, On the use of SRIM for computing radiation damage exposure, Nucl. Instrum. Methods Phys. Res. b 310 (2013) 75-80.
[32] Standard Practice for Neutron Radiation Damage Simulation by Charged-Particle Irradiation. ASTM International, Approved by 2003.

[33] M.J. Norgett, M.T. Robinson, I.M. Torrens, A proposed method of calculating displacement dose rates, Nucl. Eng. Des 33 (1975) 50-54.
[34] Lacomit varnish and remover, 2012. http://www.agarscientific.com/lacomit-varnish-and-remover.html.
[35] M.L. Jenkins, M.A. Kirk, Characterization of Radiation Damage by Transmission Electron Microscopy, First ed., IoP, Bristol & Philadelphia, 2001.
[36] R.F. Egerton, Electron Energy Loss Spectroscopy in the Electron Microscope, Second ed., Plenum Press, New York & London, 1996.
[37] K.Arakawa, K.Ono, M.Isshiki, K.Mimura, M.Uchikoshi, H.Mori, Observation of the One-Dimensional Diffusion of Nanometer-Sized Dislocation Loops, Science 318 (2007) 956-959.
[38] D.E.J. Armstrong, X. Yi, E.A. Marquis, S.G. Roberts, Hardening of self ion implanted tungsten and tungsten 5-wt% rhenium, J. Nucl. Mater. 432 (2013) 428-436.
[39] D.E.J. Armstrong, A.J. Wilkinson, S.G. Roberts, Mechanical properties of ion-implanted tungsten–5wt% tantalum, Phys. Scr. T145 (2011) 014076.
[40] X. Yi. In-situ irradiation studies of 150 keV W+ implanted W and W-alloys: damage microstructure and thermal stability. University of Oxford, 2013.
[41] M.R. Gilbert, S.L. Dudarev, M.-C. Marinica, F. Willaime, A. Sand et al. The anomalous stability of mesoscale <100> prismatic dislocation loops in irradiated tungsten: Experiment and simulation. MRS Fall Meeting. Boston, 2012.
[42] J. Marian, B.D. Wirth, J.M. Perlado, Mechanism of Formation and Growth of 〈100〉 Interstitial Loops in Ferritic Materials, Phys. Rev. Lett. 88 (2002) 255507.
[43] K. Arakawa, H. Mori, Energetics of formation process of a prismatic dislocation loop via the collision between two 1/2 loops in α-iron, J. Phys.: Conf. Ser. 165 (2009) 012005.
[44] L.K. Keys, J. Moteff, Neutron irradiation and defect recovery of tungsten, Journal of Nuclear Materials 34 (1970) 260-280.
[45] F. Ferroni, X. Yi, K. Arakawa, S.P. Fitzgerald, P.D. Edmondson, S.G. Roberts, High temperature annealing of ion irradiated tungsten, Acta Materialia 90 (2015) 380-393.
[46] M.W. Thompson, The damage and recovery of neutron irradiated tungsten, Philos. Mag. 5 (1960) 278-296.
[47] V.N. Bykov, G.A. Birzhevoi, M.I. Zakharova, V.A. Solov'ev, Nature and thermal stability of radiation defects in single-crystal tungsten, At. Energ. 33 (1972) 930-935.
[48] W.H. Zhou, C.G. Zhang, Y.G. Li, Z. Zeng, Creeping Motion of Self Interstitial Atom Clusters in Tungsten, Sci. Rep. 4 (2014)
[49] M.R. Gilbert. BCC metals in extreme environments: modelling the structure and evolution of defects. Materials, Doctor of Philosophy. Oxford: University of Oxford, 2009.
[50] P. Ehrhart, P. Jung, H. Schultz, H. Ullmaier, Landolt-Bornstein: Atomic Defects in Metals, ed., Springer-Verlag, Berlin, 1991.
[51] S.L. Dudarev, M.R. Gilbert, K. Arakawa, H. Mori, Z. Yao, M.L. Jenkins, P.M. Derlet, Langevin model for real-time Brownian dynamics of interacting nanodefects in irradiated metals, Phys. Rev. B. 81 (2010) 224107.
[52] M. Kiritani, N. Yoshida, H. Takata, Y. Maehara, Growth of Interstitial Type Dislocation Loops and Vacancy Mobility in Electron Irradiated Metals, J. Phys. Soc. Japan. 38 (1975) 1677-1686.
[53] S.I. Golubov, A.V. Barashev, R.E. Stoller, Radiation damage theory, First, Elsevier, 2012, pp.357-391.
[54] C.H. Woo, A.A. Semenov, Dislocation climb and interstitial loop growth under cascade damage irradiation, Philos. Mag. A. 67 (1993) 1247-1259.
[55] S.L. Dudarev, Density Functional Theory Models for Radiation Damage, Annu. Rev. Mater. Res. 43 (2013) 35-61.

[56] B. Navinšek, V. Marinkovič, M. Osredkar, G. Carter, Radiation damage, annealing and thermal desorption in tungsten induced by low energy A+ ion bombardment, Radiat. Eff. 3 (1970) 115-121.
[57] D. Kaoumi, J. Adamson, Self-ordered defect structures in two model F/M steels under in situ ion irradiation, J. Nucl. Mater. 448 (2014) 233-238.
[58] J.B. Whitley, G.L. Kulcinski, P. Wilkes, H.V. Smith Jr, The depth dependent damage profile in nickel irradiated with nickel or copper ions, J. Nucl. Mater. 79 (1979) 159-169.
[59] S.L. Dudarev, K. Arakawa, X. Yi, Z. Yao, M.L. Jenkins, M.R. Gilbert, P.M. Derlet, Spatial ordering of nano-dislocation loops in ion-irradiated materials, J. Nucl. Mater 455 (2014) 16-20.
[60] W. Jäger, M. Rühle, M. Wilkens, Elastic interaction of a dislocation loop with a traction-free surface, Phys. Stat. Sol. (a) 31 (1975) 525-533.
[61] M. Muzyk, D. Nguyen-Manh, K.J. Kurzydłowski, N.L. Baluc, S.L. Dudarev, Phase stability, point defects, and elastic properties of W-V and W-Ta alloys, Phys. Rev. B 84 (2011) 104115.
[62] J.P. Hirth, J. Lothe, Theory of dislocations, Second ed., Krieger, Malabar, Florida, 1982.
[63] M. Griffiths, M.H. Loretto, R.E. Smallman, Electron damage in zirconium: I. defect structure and loop character, J. Nucl. Mater. 115 (1983) 313-322.
[64] M. Griffiths, M.H. Loretto, R.E. Smallman, Electron damage in zirconium: II. Nucleation and growth of c-component loops, J. Nucl. Mater. 115 (1983) 323-330.
[65] J.H. Evans, Radiation-induced shrinkage of voids in molybdenum and TZM, Nature 278 (1979) 728-729.
[66] D.B.Williams, C.B.Carter, Transmission electron microscopy: A text book for materials science (I-IV), First ed., Springer-Verlag, 1996.
[67] T.W. Ridler, S. Calvard, Picture thresholding using an iterative selection method, IEEE Trans. Syst. Man. Cybern. SMC-8 (1978) 630-632.
[68] P. Hirsch, A. Howie, R. Nicholson, D.W. Pashley, M.J. Whelan, Electron microscopy of thin crystals, 2nd Revised ed., Krieger, Malabar, Florida, 1977.
[69] K. Yabuuchi, M. Saito, R. Kasada, A. Kimura, Neutron irradiation hardening and microstructure changes in Fe–Mn binary alloys, J. Nucl. Mater. 414 (2011) 498-502.
[70] A. Prokhodtseva, B. Décamps, A. Ramar, R. Schäublin, Impact of He and Cr on defect accumulation in ion-irradiated ultrahigh-purity Fe(Cr) alloys, Acta. Mater. 61 (2013) 6958-6971.

Table 1. Summary of irradiation conditions.

Material	Temperature (°C)	Dose (W^+/m^2)	dpa	dpa/s
W	300	3.3×10^{17}	0.4	3×10^{-4}
		10^{18}	1.2	
		2.5×10^{19}	30	
	500	3.3×10^{17}	0.4	
		10^{18}	1.2	
		3×10^{18}	3.6	
	[a] 750	10^{18}	1.2	
W-5Ta	300	3.3×10^{17}	0.4	
		10^{18}	1.2	
	500	10^{18}	1.2	
		3×10^{18}	3.6	
W-5Re	300	3.3×10^{17}	0.4	
		10^{18}	1.2	
	500	3.3×10^{17}	0.4	
		10^{18}	1.2	
		3×10^{18}	3.6	

[a] Implantation performed with 1.9 MeV W^+ ions (Sandia). All others were carried out with 2.0 MeV W^+ ions (Surrey).

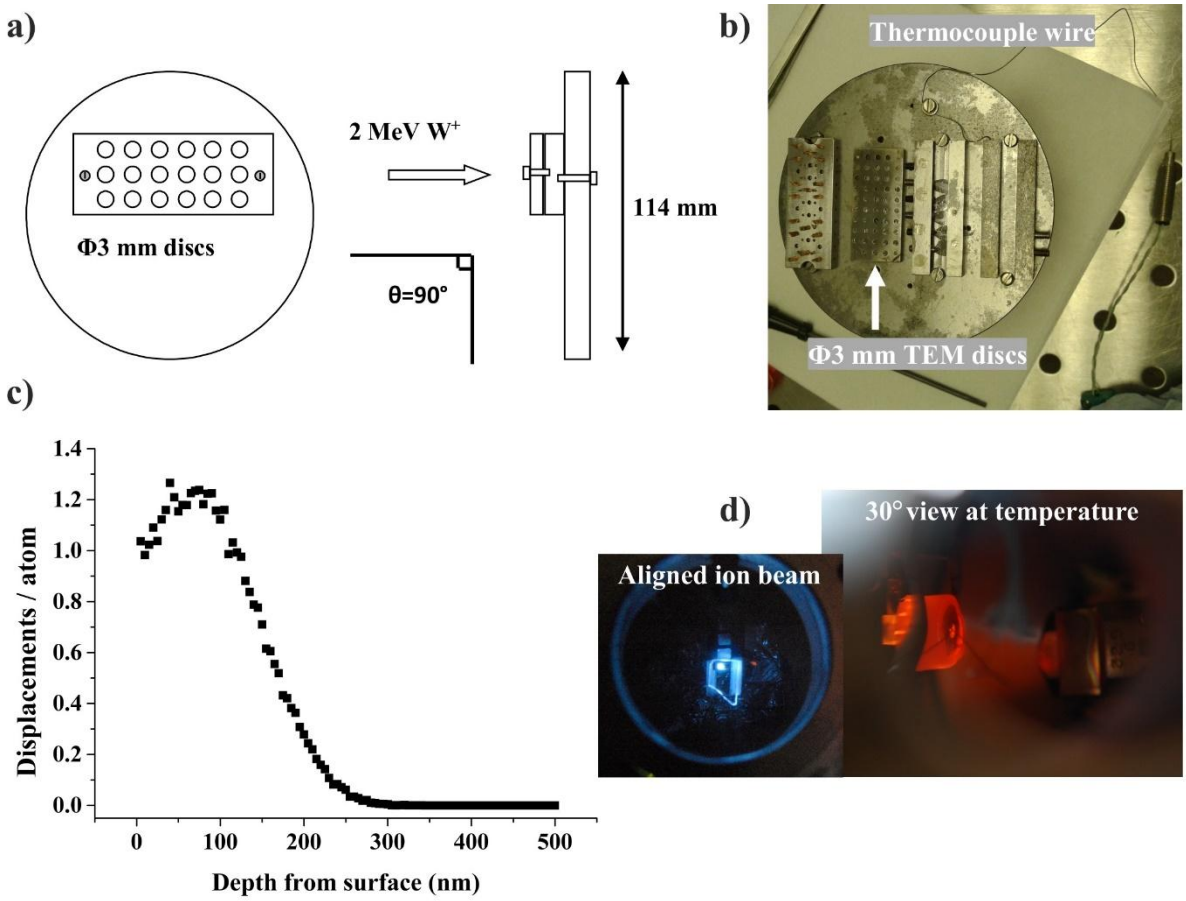

Fig. 1. Ion implantation experimental configurations: (a) A schematic illustration of the 2 MeV W^+ ion beam geometry with respect to the specimens and (b) the base plate design at the National Ion Beam Centre, University of Surrey (UK). (c) The damage profile of 2 MeV W^+ ions calculated by SRIM 2013 for a fluence of 10^{18} W^+/m^2. Displacement threshold energy: 90 eV [29, 31]. (d) View of the end station at Sandia National Laboratories utilized for 1.9 MeV ion irradiation during ion beam alignment (blue) and at 30° to the beam line during irradiation with the stage at elevated temperature (red).

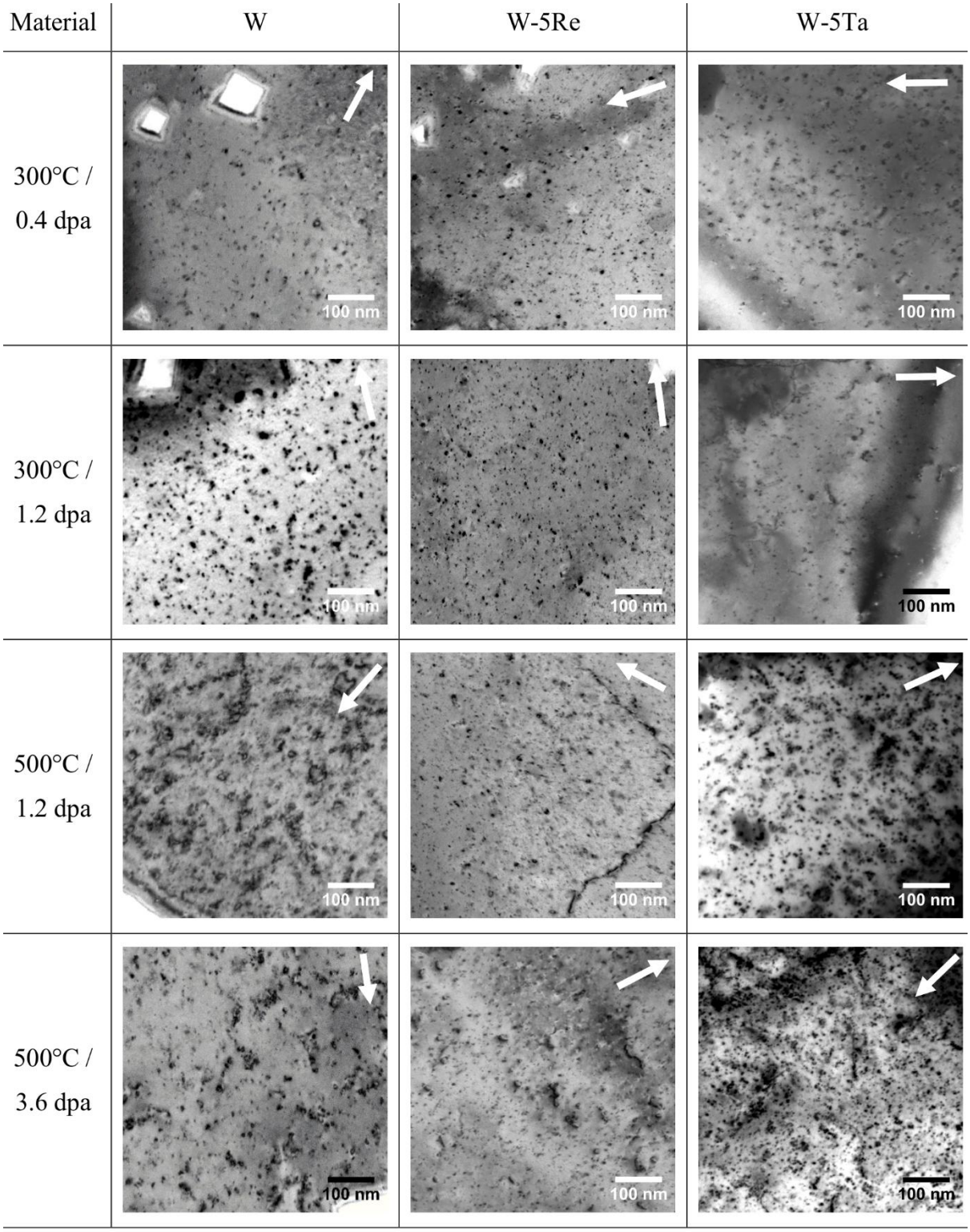

Fig. 2. Selected micrographs illustrating the damage microstructure in W and alloys as a function of irradiation temperature and dose. All images were recorded from **z** = <001> oriented grains under two-beam kinematical bright-field condition using **g** = 200 (indicated by white arrows).

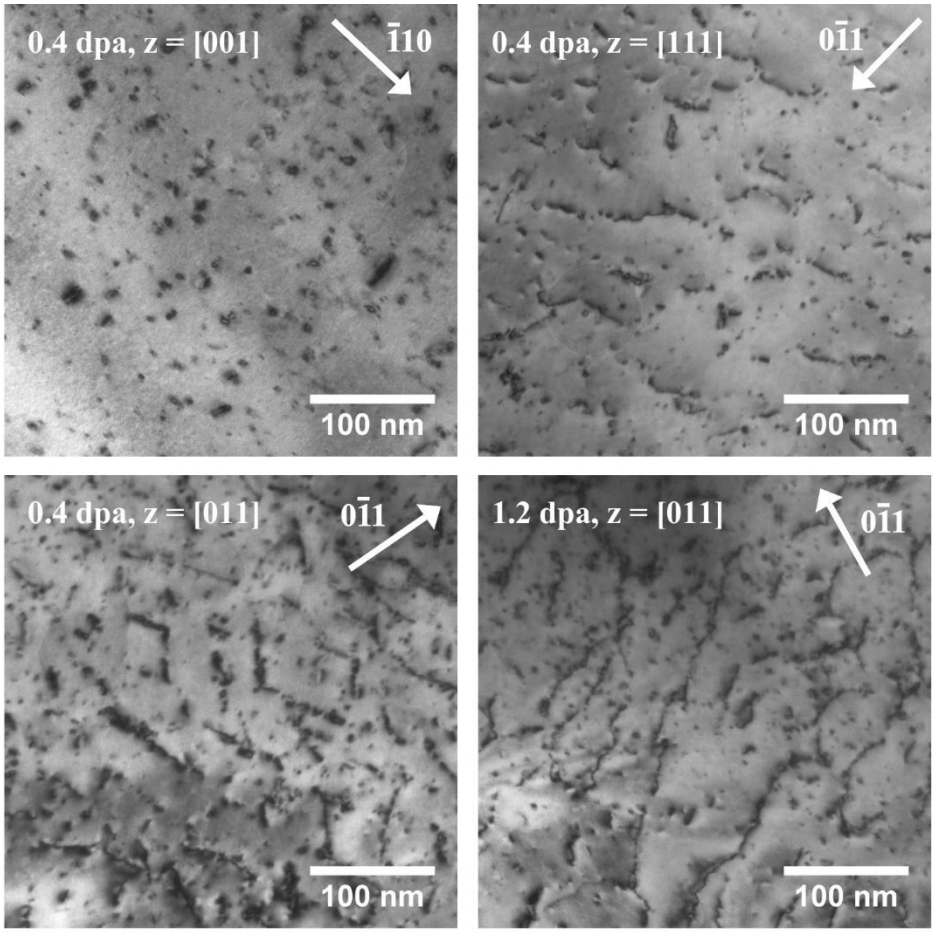

Fig. 3. Comparison of damage microstructures in W-5Ta, irradiated at 300°C in **z** = [001], [011] and [111] orientations.

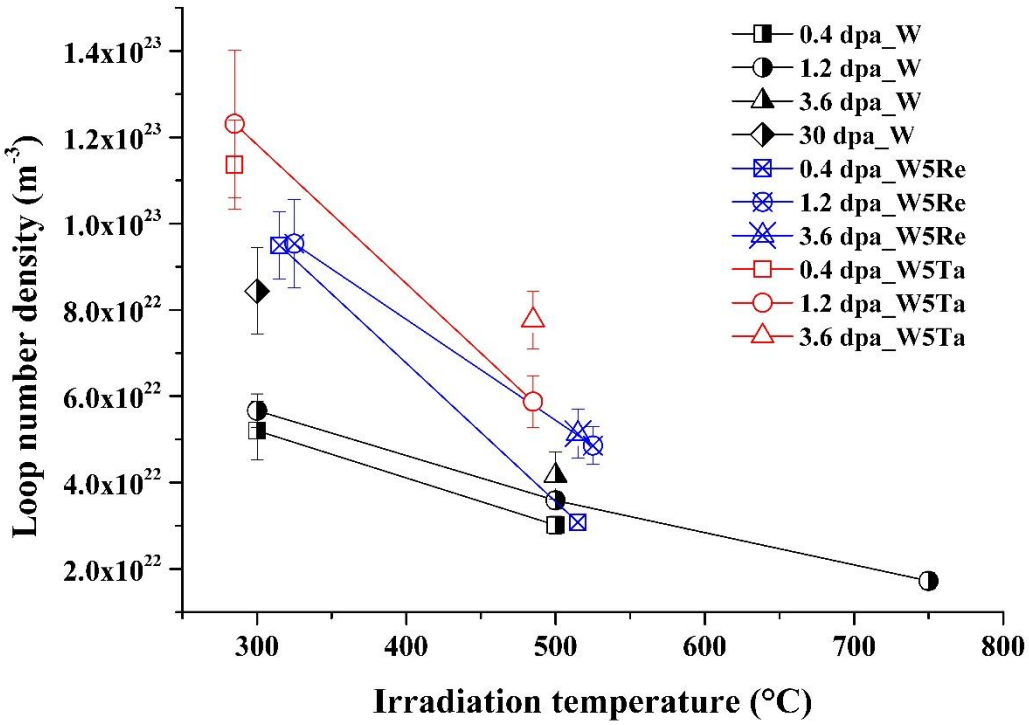

Fig. 4. Loop volume number density in pure W, W-5Re and W-5Ta plotted as a function of irradiation temperature and dose. For the purpose of clarity, data points have been shifted by ±15°C on the temperature axis so as to separate data points for each irradiation condition.

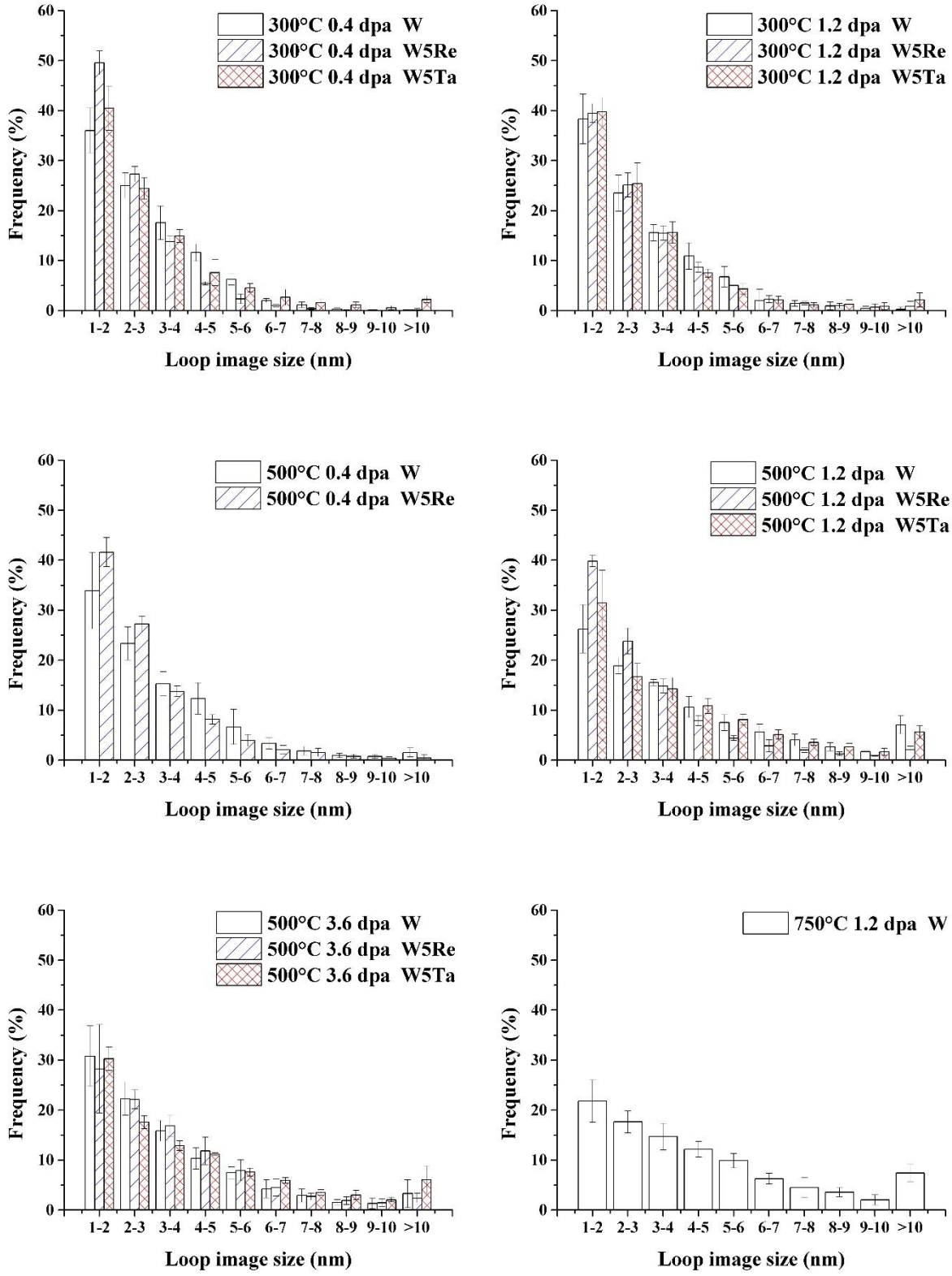

Fig. 5. Loop size distributions in pure W, W-5Re and W-5Ta plotted as a function of irradiation temperature and dose. The number of loops sampled for loop sizing for each condition was typically on the order of 1000. Loops with diameters larger than 10 nm are grouped as one category. No loops exceeded 20 nm in diameter.

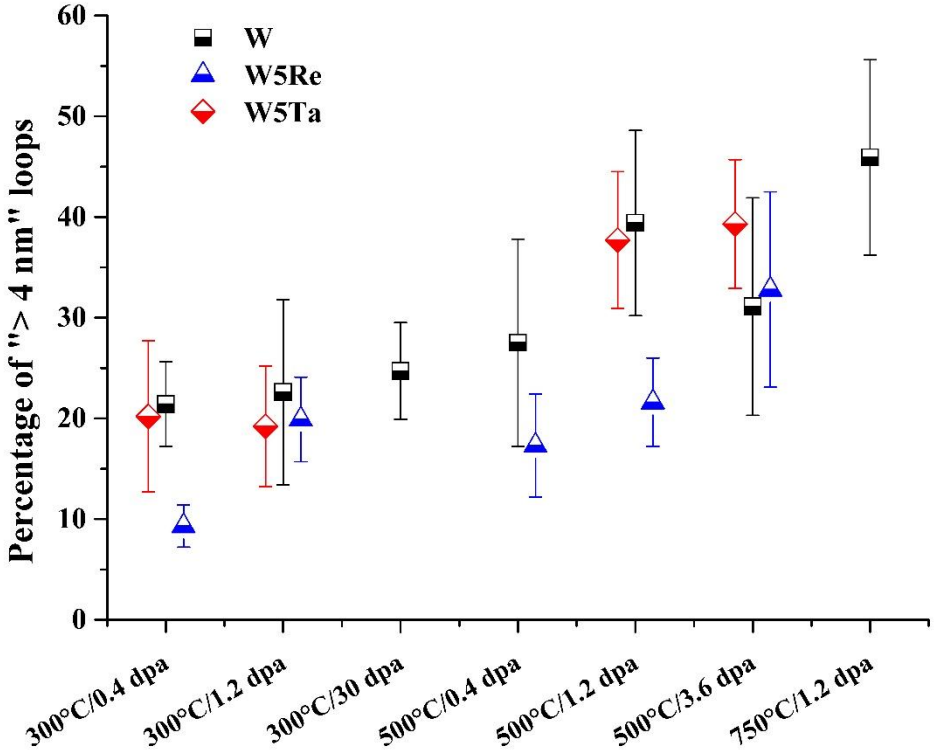

Fig. 6. The variation of the fraction of loops larger than 4 nm with irradiation condition and material composition.

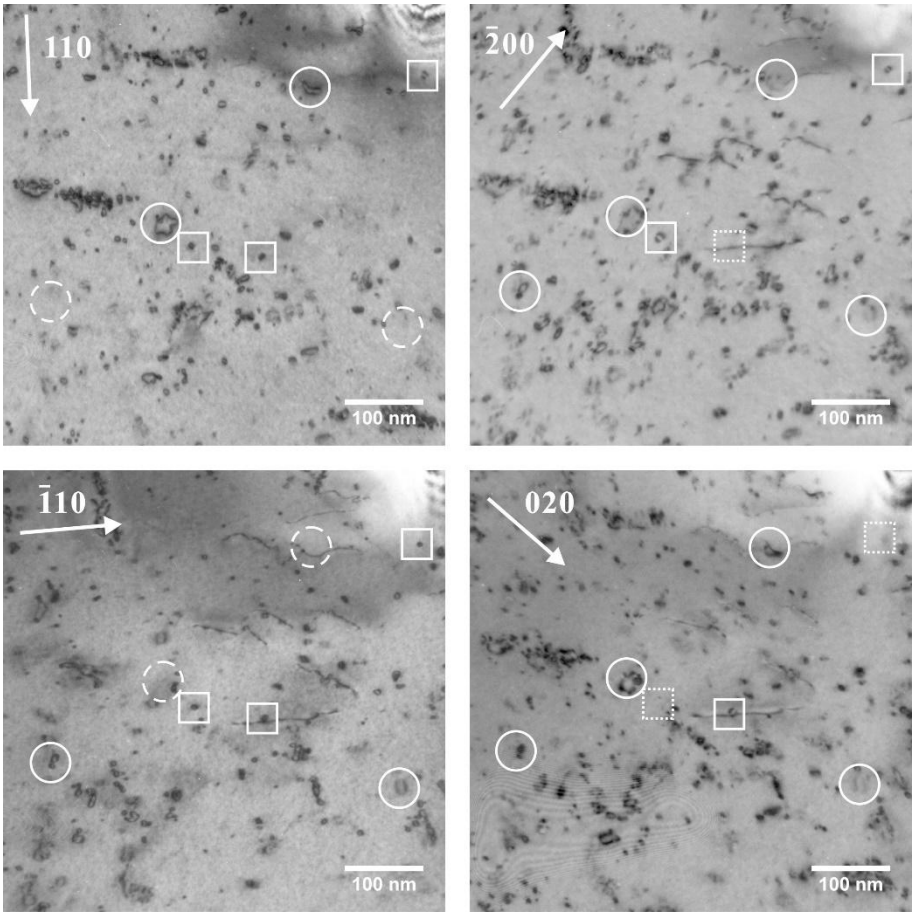

Fig. 7. Pure W irradiated with 1.9 MeV W^+ ions at 750°C at a dose of 1.2 dpa. Images were taken from the same area of interest, but under different diffraction conditions. Both ½<111> (circular marks) and <100> (square marks) dislocation loops were identified, and solid/dashed lines represent their visibility/invisibility with respect to the diffraction condition. Detailed analyses (Burgers vector variant and nature) were performed based on weak-beam dark-field micrographs.

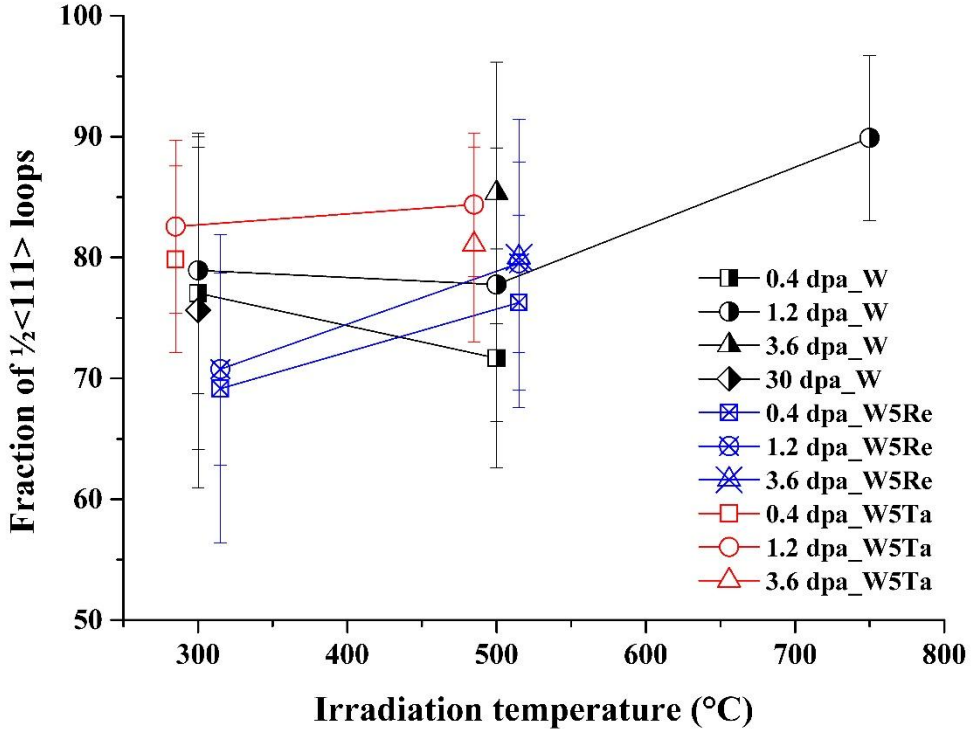

Fig. 8. Fraction of ½<111> loops in W/W-alloys plotted against temperature and dose.

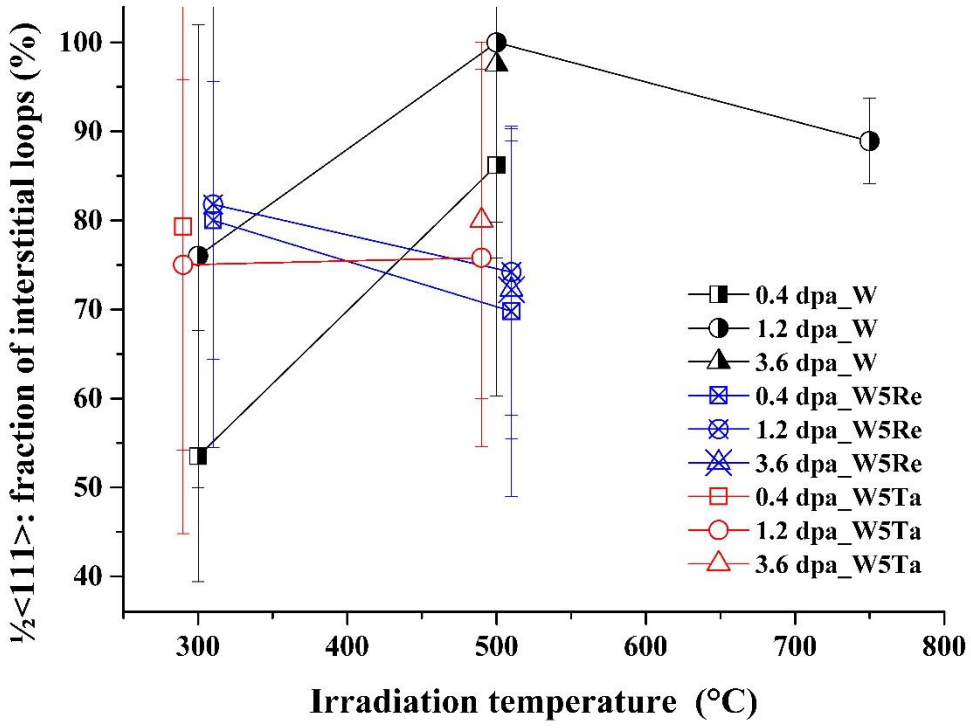

Fig. 9. The fraction of interstitial loops among loops with **b** = ½<111> in pure W, W-5Re and W-5Ta, as a function of irradiation temperature and dose.

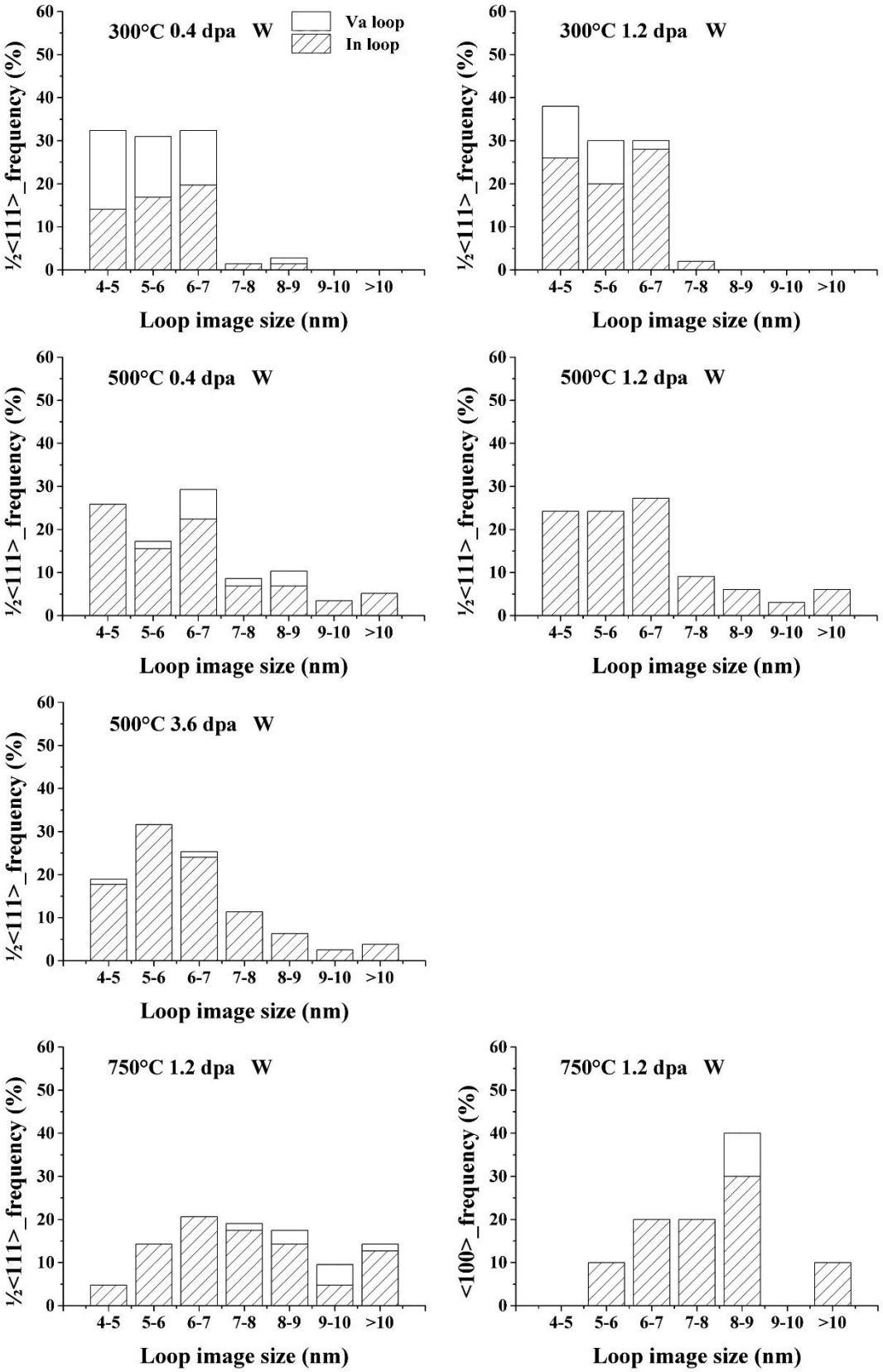

Fig. 10. The size distributions of interstitial/vacancy-type dislocation loops in pure W, normalized against the total sampled loop population, i.e. 50-70 loops for **b** = ½<111> while 10 loops for **b** = <100>.

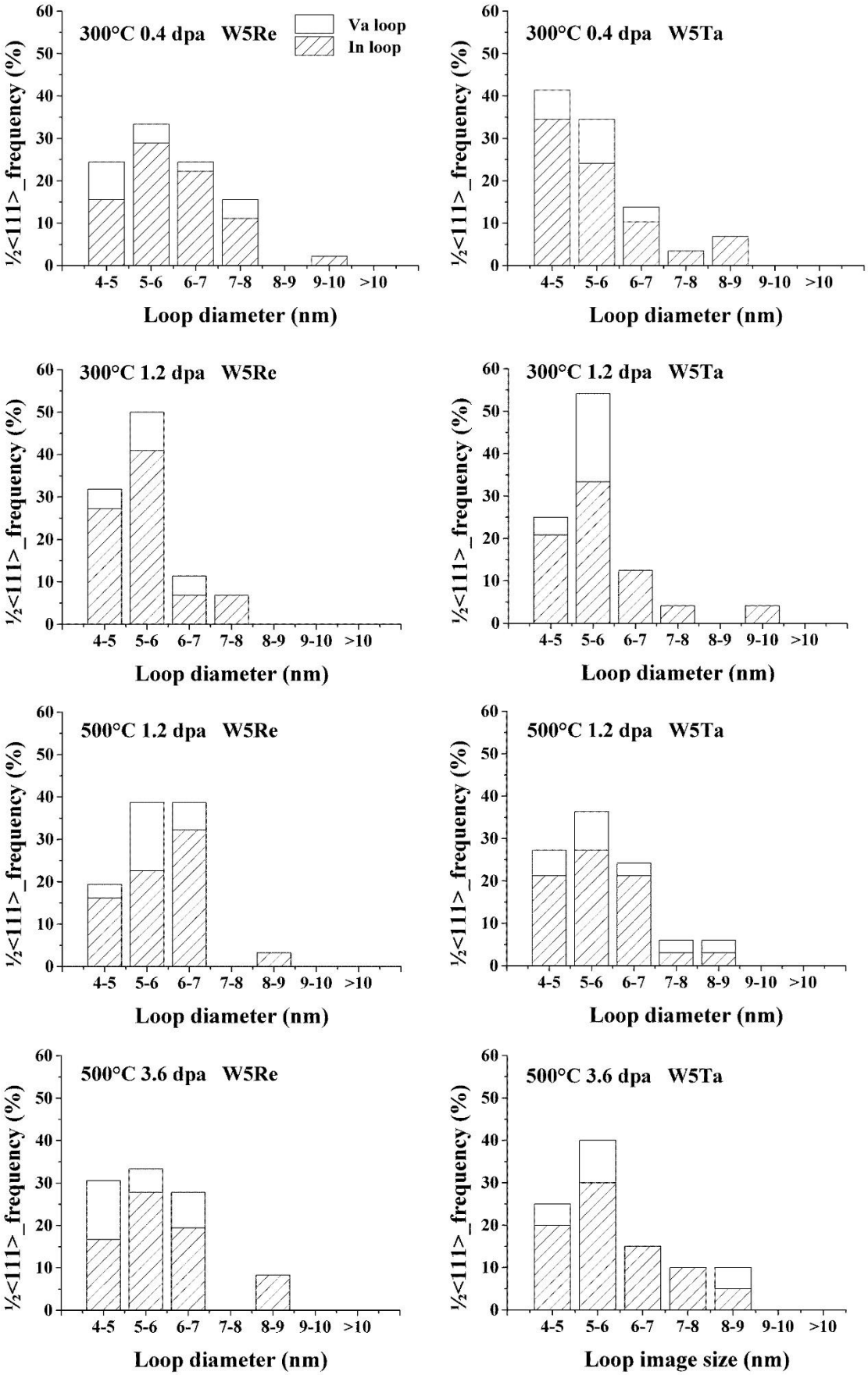

Fig. 11. The size distributions of interstitial/vacancy-type ½<111> dislocation loops in W-5Re and W-5Ta, normalized against the sampled loop population (30-70 loops).

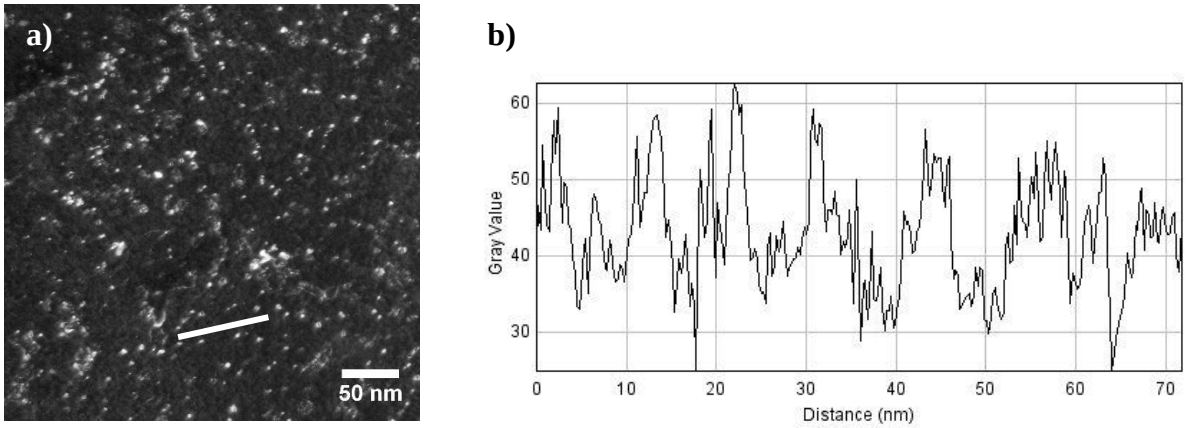

Fig. 12. Estimation of the range of loop count uncertainty: (a) a sample micrograph for image processing, obtained from an irradiated W specimen under weak-beam dark-field condition; (b) Image J generates a line profile of the selected background region (marked with a solid line). The intensity fluctuates around ±10 in arbitrary grey value units.

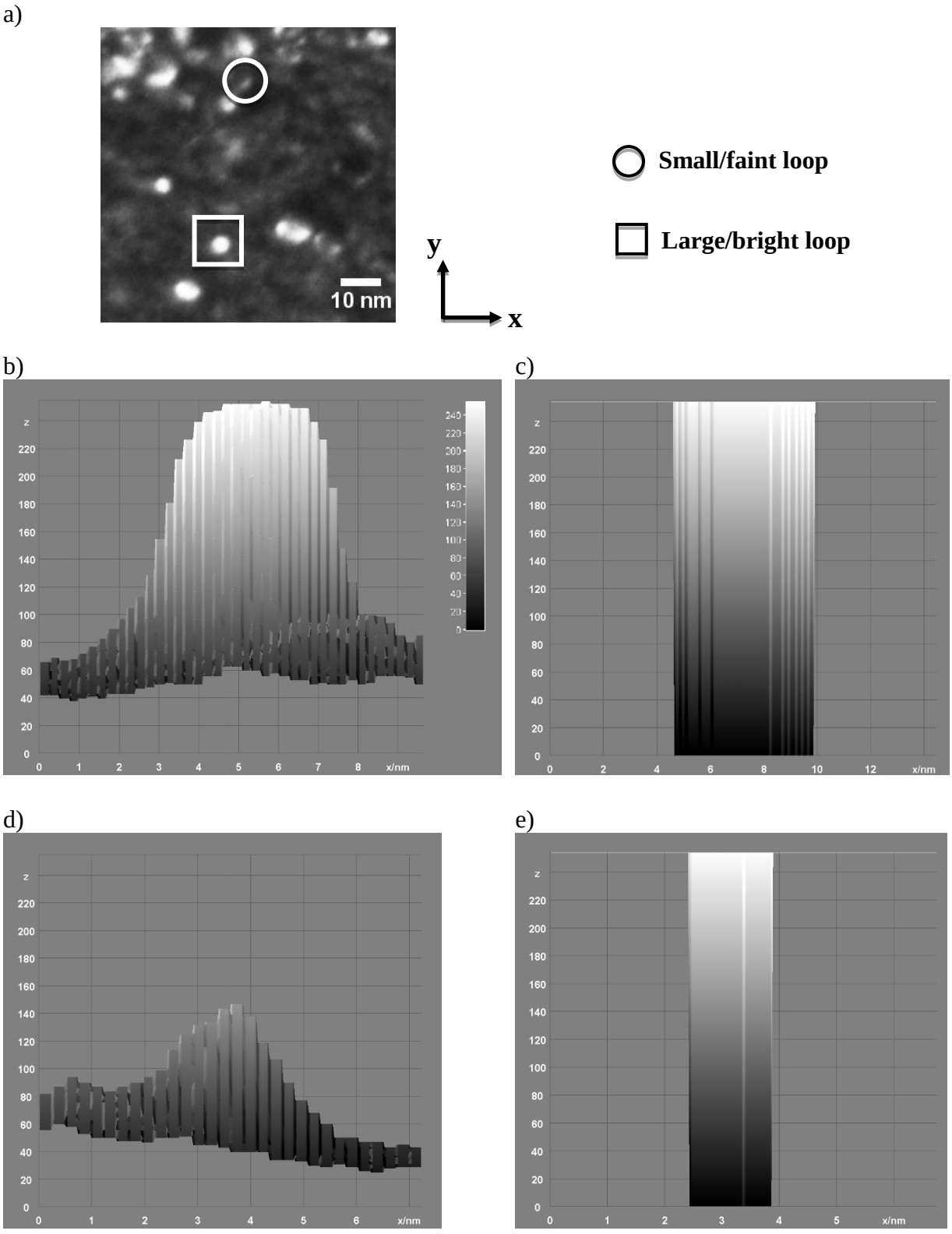

Fig. 13. Demonstration of loop sizing in an irradiated pure W specimen with 3D surface plots constructed on the same intensity scale (viewed in the x – z "intensity" plane) [65]: (a) the original grey scale image; 3D surface plots profiles of a large/bright loop in (b) grey scale and (c) binary format respectively; 3D surface plots profiles of a small/faint loop in (d) grey scale and (e) binary format respectively.